THE JOURNAL OF PHYSICAL CHEMISTRY C
A JOURNAL OF THE AMERICAN CHEMICAL SOCIETY

pubs.acs.org/JPCC

Article

Experimental Analysis of the Elastic Moduli of Atomically Thin Transition Metal Dichalcogenides

Alem Teklu, Noah Kern, Narayanan Kuthirummal, Joe Tidwell, Maxwell Rabe, Yu Gong, Wenkai Zhang, and Luis Balicas*

Cite This: https://doi.org/10.1021/acs.jpcc.4c03861

Read Online

ACCESS | Metrics & More | Article Recommendations | Supporting Information

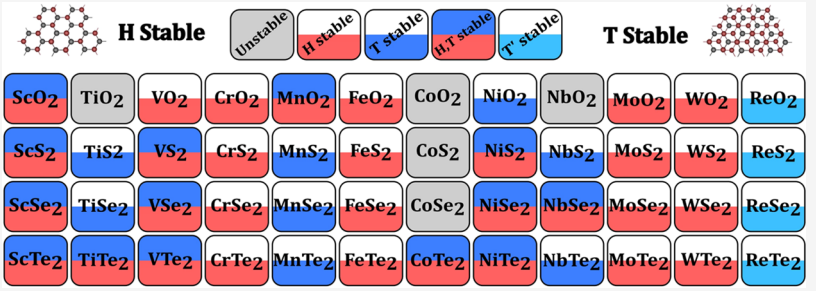

ABSTRACT: Nanoindentation was used to measure the nanomechanical properties of four two-dimensional transition metal dichalcogenides (TMDs), namely molybdenum disulfide (MoS_2), rhenium disulfide (ReS_2), rhenium diselenide ($ReSe_2$), and tungsten diselenide (WSe_2), with very high tensile strengths comparable to graphene. These materials have potential applications for new electronic device applications, but their nanomechanical properties have not yet been well studied. For this purpose, an atomic force microscope (AFM) capable of measuring the elastic moduli of these two-dimensional nanomaterials through nanoindentation was used to generate force−distance curves for analysis. In this work, we developed a new Python code to analyze these force−distance curves, resulting in more accurate values of the reduced Young's modulus and stiffness of each of these nanomaterials as compared to existing data analysis software such as AtomicJ and MountainsSPIP. The values obtained using our code for reduced Young's modulus of MoS_2, ReS_2, $ReSe_2$, and WSe_2 were 140, 79, 37, and 38 GPa, respectively, with percent differences as summarized in Table 3. Among the samples, MoS_2 has the highest values for its reduced Young's modulus and stiffness followed by, in order, ReS_2, WSe_2, and $ReSe_2$. Our results were in better agreement with theoretical calculations in the literature than those obtained by the other two pieces of data analysis software.

INTRODUCTION

As the field of electronics advances through the use of 2D materials, the search for graphene-like materials is getting increased attention, along with growing interest in transition metal dichalcogenides (TMDs). Of these materials, there is interest in the use of MoS_2, ReS_2, $ReSe_2$, and WSe_2 for new electronic device applications. MoS_2 and $ReSe_2$ are both semiconductors with monolayer bandgaps of 1.8 and 1.17 eV, respectively, with MoS_2 having potential use in optoelectronics and $ReSe_2$ for use in flexible electronics.[1,2] Monolayer ReS_2 also has a similar band gap of 1.35−1.44 eV and has shown potential for use in optoelectronics, energy harvesting, and storage, and other electrical applications, such as field effect transistors.[3,4] WSe_2 has a direct band gap of 1.65−2.1 eV when monolayer[5,6] with potential applications in functional electronics and optoelectronics. The electrical and optical properties of the four TMD materials listed above are widely researched. Despite many theoretical studies, there has not been much experimental work on the nanomechanical properties of these TMDs. In addition, existing force curve analysis packages have been unreliable in producing accurate nanomechanical properties of these TMDs due to the complexity of the measured force curve fitting process. None of the existing imaging techniques can accurately determine the contact area, A_c, between the AFM probe and sample, which is an important factor in the calculations of nanomechanical parameters. Oliver and Pharr's method of determining the reduced Young's modulus is the most commonly used method for a perfect geometry of the AFM tip by employing a simple relationship between the projected contact area and the indentation depth. However, there are very few publicly available software packages that use this method, with many employing models based on tip geometry

Received: June 11, 2024
Revised: October 30, 2024
Accepted: October 31, 2024

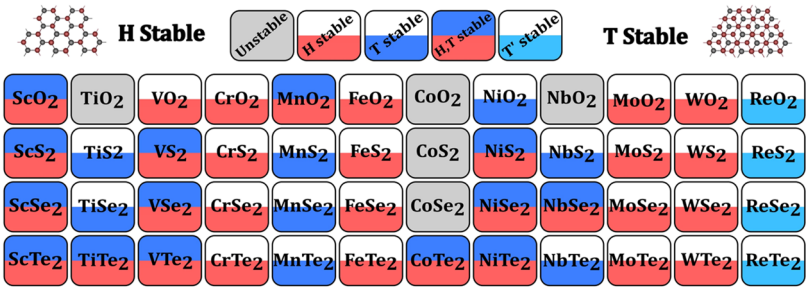

Figure 1. List of known TMDs and the 2D layered structure (2H structure, 1T structure, or 1T' structure) in which each is stable.[10]

with larger deviations from the ideal shape, leading to larger inaccuracies in the contact area and, hence, nanomechanical parameters. In this work, a program was written in Python using widely available modules to allow more control over the curve-fitting process as well as accurate identification of the probe's contact point and area and the use of the Oliver and Pharr method.

Monolayer graphene is an exceptionally hard material. It has been reported that monolayer graphene has a very high value of Young's modulus in the range of 0.89−1.0 TPa.[7,8] However, graphene's zero band gap makes it unsuitable for some of the applications listed above.[9] Theoretical calculations of monolayer TMDs exhibit a high value of Young's modulus similar to that of graphene, and they are more suitable for optoelectronic applications than graphene. As some of these materials are used for nanodevice fabrication as two-dimensional lateral heterostructures, layering of these materials exerts significant stress, affecting mechanical properties such as Young's modulus, stiffness, hardness, and roughness of these TMDs. Therefore, in this work, we developed a Python code analysis software to analyze our experimental data - force-distance curves obtained by nanoindentation coupled with atomic force microscope imaging (AFM) to understand the nanomechanical properties of these TMDs better. The values of reduced Young's modulus and stiffness obtained using our Python code were compared with results obtained by other analysis software packages like AtomicJ and MountainsSPIP. These values were also compared to values obtained by theoretical and computational analysis.

The general formula for layered transition metal dichalcogenides (TMDs) is MX_2, where M represents a transition metal, and X stands for chalcogen. About 88 different combinations of MX_2 compounds have been identified, and 52 of them can be stable in free-standing, single-layer honeycomb-like structures based on stability analysis using first-principle calculations of structure optimization, phonon frequency, formation energy, elastic properties, and finite temperature ab initio molecular dynamics calculations as shown in Figure 1.[10] In Figure 1, we modified the table of TMDs created by Ataca et al.[10] to include four additional TMDs to the list, namely, ReS_2, $ReSe_2$, $ReTe_2$, and ReO_2, two of which were synthesized and studied in this work. Interatomic bonding in all these TMD compounds is covalent, with each chalcogen forming two covalent bonds with neighboring atoms. However, the interlayer coupling is a weak van der Waals interaction, and monolayer or few-layer two-dimensional TMDs can be easily exfoliated. Subsequently, the band gap can be engineered for various device applications by varying the number of layers.[11]

Young's modulus, also called the elastic modulus, is a measure of the stress-to-strain ratio of a material, where stress is the force per unit area and strain is a measure of deformation in the material. Young's modulus can also be expressed in terms of the elastic constants.

Hardness is a measure of the resistance to deformation caused by a surface indentation and is proportional to the applied load and area of indentation.[12] Stiffness, while similar to hardness, measures the material's resistance to deformation from an applied force and is defined as the relationship between the applied force and the deformation of the material.[12] Our focus was to perform detailed experimental measurements in order to accurately determine the nanomechanical properties of each of these four TMD materials. We developed a new Python code to accurately determine the Young's modulus and stiffness in order to compare their values to the Young's modulus of monolayer graphene, each other, and the expected theoretical predictions as well as experimental values from other sources.

Nanoindentation is one of the most common means of testing the nanomechanical properties of materials. Once calibrated, the atomic force microscope (AFM) measures the intensity of interactions between a probe and the sample during the loading stage (indentation) and the unloading stage (while the probe is retracted). The small area of the probe tip, which comes in various shapes, allows for a high sensitivity to minuscule forces. The probe tip is placed on a soft spring (cantilever), which is often made of silicon, allowing for detecting forces in the range of a few nN. Figure 2 shows the

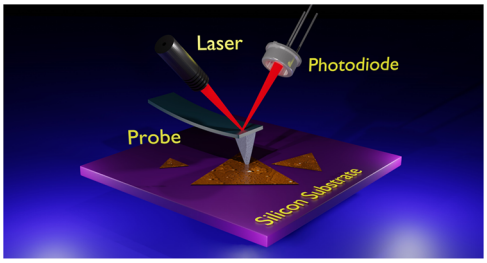

Figure 2. Basic components of an AFM: probe tip, cantilever, laser, and photodiode.

basic components of the AFM showing the indentation of the samples and the resulting deflection of the incident laser. The indentation is recorded as force−distance curve as shown in Figure 3 that is similar to the force−distance curve behavior originally proposed by Oliver and Pharr[13] in Figure 4.

From this curve, numerous nanomechanical properties of thin films and other related characteristics can be obtained. We

https://doi.org/10.1021/acs.jpcc.4c03861
J. Phys. Chem. C XXXX, XXX, XXX−XXX

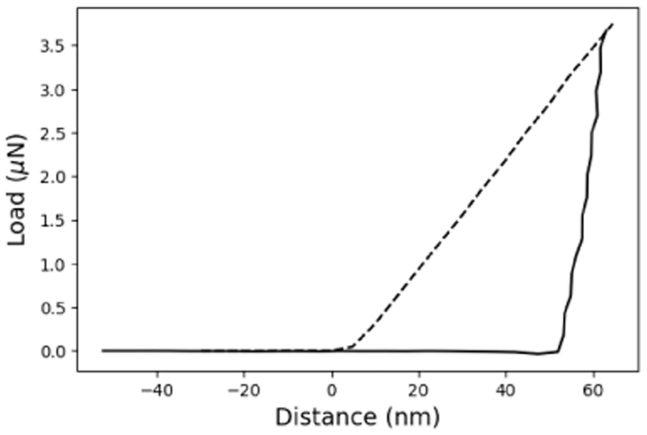

Figure 3. Force−distance curve for ReS_2 exhibiting plastic deformation. The dashed curve represents the loading curve, while the solid curve represents the unloading curve.

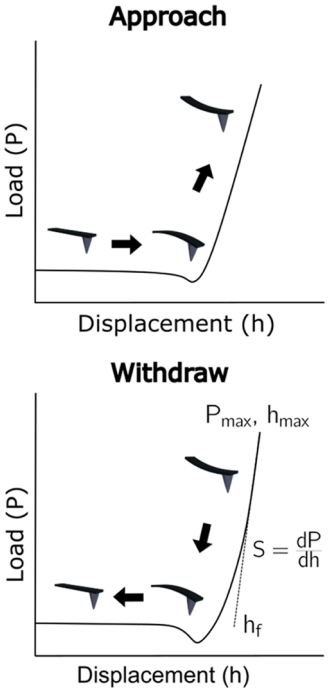

Figure 4. A sketch of the theoretically predicted force curve similar to the one given in ref 13.

have employed eqs 1, 2, 6, and 8 that can be used to analyze the data to obtain the stiffness and Young's modulus.

As seen in Figure 4, contact stiffness, S, is defined to be the slope of the unloading curve. Because the upper portion of the unloading curve corresponds to the linear stage of the probe retraction before tapering off, the most accurate stiffness measurements are calculated from this initial gradient. Mathematically

$$S = \left(\frac{\partial P}{\partial h}\right)_{h=h_{max}} \tag{1}$$

where P is the force and h is the displacement.

According to Oliver and Pharr,[13] the unloading force P is not linearly dependent on the indentation depth h; rather, it is approximated by the power law relation:

$$P = \alpha(h - h_f)^m \tag{2}$$

where α and m are power law fitting constants and h_f is the final depth or the permanent deformation caused by the indentation.

Figure 5 shows a cross-sectional view of an ideal indentation process to visualize the contact depth, h_c, and subsequent

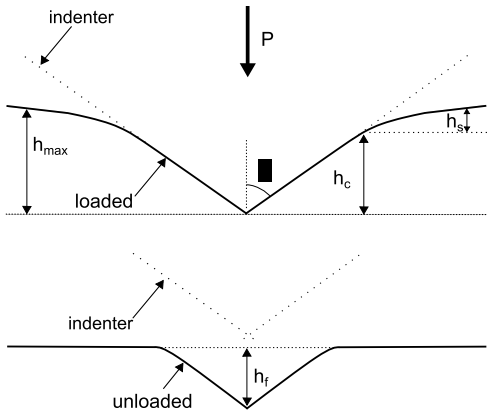

Figure 5. Cross-sectional view of an ideal indentation during indentation and after the tip has withdrawn.

projected cross-sectional area given by eq 5. The contact depth h_c can be expressed as

$$h_c = h_{max} - h_s \tag{3}$$

and h_s is

$$h_s = \epsilon\left(\frac{P_{max}}{S}\right) \tag{4}$$

where h_{max} is the maximum contact depth, h_s is the sink-in depth, P_{max} is the maximum applied force, S is the stiffness, and ϵ is a geometric constant relating the probe shape ($\epsilon = 0.75$ for conical tip indenter). Similarly, the projected contact area is given by

$$A(h_c) = (\pi)[\tan(\theta)(h_c)]^2 \tag{5}$$

Here θ refers to the half angle of the probe tip. The variable h_c is the contact depth and it is the difference between the maximum displacement and the depth of the permanent deformation. Using the value of the half angle for the conical probe used in this work, the contact area can be calculated as

$$A(h_c) = (\pi)[\tan(18^\circ)(h_c)]^2 \tag{6}$$

Once the contact area is determined, the hardness, H, defined as the mean pressure a substance can support across that area, is calculated using the equation

$$H = \frac{P_{max}}{A(h_c)} \tag{7}$$

where P_{max} is the max load (N), and A (m^2) is the contact area during indentation.[12]

Young's modulus is a measure of elasticity or the stress-to-strain ratio of a substance. Because of the elastic nature of the probe (that is, it is not infinitely rigid), only the reduced or effective Young's modulus can be calculated.[14] Using the stiffness from eq 1 and the contact area from eq 6, the reduced elastic modulus takes elastic deformations in both the probe and sample into account and is given by

https://doi.org/10.1021/acs.jpcc.4c03861
J. Phys. Chem. C XXXX, XXX, XXX−XXX

$$E_r = \frac{S\sqrt{\pi}}{2\sqrt{A(h_c)}} \tag{8}$$

where E_r is the reduced Young's modulus (Pa). During the nanoindentation process, both the probe tip and sample suffer mechanical deformations, hence, the reduced Young's modulus is determined. If the Young's modulus E_i and the Poisson's ratio ν_i of the indenter are known, then the reduced Young's modulus of the sample can be calculated using the relation:

$$\frac{1}{E_r} = \frac{1-\nu^2}{E} + \frac{1-\nu_i^2}{E_i} \tag{9}$$

Using the Oliver and Pharr model, three main characteristics must be measured from the force−distance curve in order to determine Young's modulus: the maximum applied load, P_{max} (nN), the displacement at P_{max}, h_{max} (nm), and the contact stiffness, S. Once these quantities are measured, the projected cross-sectional area of the indenter, $A(h_c)$ (m^2), can be calculated using h_c, the residual contact depth, and a conical approximation of the probe's dimensions using the manufacturer's specifications. Figure 6 is a scanning electron microscope (SEM) image of the AFM probe showing its conical shape.

METHODS

A Nanosurf FlexAFM was used to image and indent the samples in conjunction with the Nanosurf Easyscan 2 software. A diamond doped probe (DD-ACTA) (Figure 6) was mounted to the scan head of the atomic force microscope. A laser deflects off of the tip of the probe and onto a photodiode. Changes in the probe's deflection will cause a change in the current produced by the photodiode (Figure 2). The deflection sensitivity and spring constant of the cantilever must be known to accurately determine the force of the indentation. In eq 10, N is the force of the indentation, $\frac{m}{V}$ is the maximum deflection of the probe, V is the deflection voltage, and $\frac{N}{m}$ is the spring constant of the cantilever.

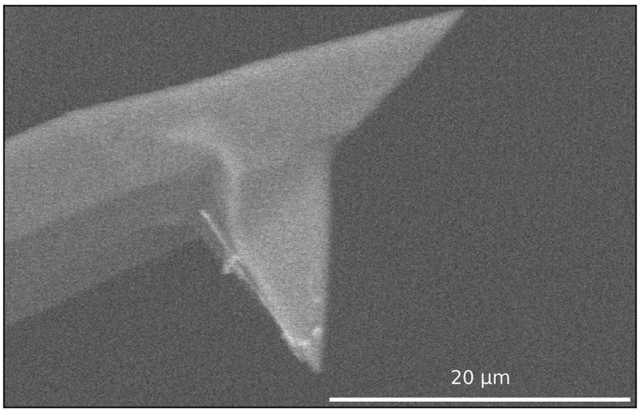

Figure 6. Scanning electron microscopy (SEM) image of the indenter tip.

$$N = (V)\left(\frac{m}{V}\right)\left(\frac{N}{m}\right) \tag{10}$$

The probe's resonant frequency must be known in order to find its spring constant. The manufacturer of the probe (AppNano) provided an estimate of the resonant frequency at 300 kHz, so a coarse frequency sweep was performed between 200 and 600 kHz in steps of 100 Hz. The resonant peak was selected, and a fine sweep was performed ranging from 407 to 409 kHz. The resonant frequency was approximately 408 kHz across every trial. The software uses the Sader method to find the spring constant based on the resonant frequency, Q-factor, geometry of the cantilever, and the density of air.[15,16]

The maximum deflection can be found by determining the deflection sensitivity which is used to equate the voltage produced by the photodiode to the deflection of the probe. In order to accurately determine the maximum deflection, the probe must indent a material with a stiffness significantly greater than its own stiffness. Therefore, sapphire was used for this calibration due to its hardness. The sapphire was indented five times while the resultant force curves were generated. The software automatically selects four of the best force curves for this calibration. The first 70% of the unloading curves were fit in order to determine the deflection sensitivity. The maximum deflection is then found by dividing the scale of the AFM detector (10 V) by the deflection sensitivity.

Imaging of the samples was performed in Dynamic mode, while indentation was performed in Static mode. In Dynamic mode, the probe is oscillated close to its resonant frequency by a piezo shaker. The amplitude of the oscillation will decrease as the probe comes closer to the surface of the sample. This enables the AFM to record the topography of the sample.[17]

Nanoindentation was performed in Static mode. The probe would start 5 μm above the surface of the sample. It would approach and indent with a max load of 3 to 5 μN before retracting to its starting point. The total time between reaching the surface and indenting completely was 2 s. Additionally, the withdrawal from max load to the surface of the sample took 2 s. Indentation was performed 16 times at different locations on a 4 × 4 grid on a uniform region of approximately 100 × 100 nm^2. Measurements were performed on 5−6 samples of each TMD. For each sample, indentations were done on several sets 4 × 4 grids. The values of reduced Young's modulus, which were obtained by these nanoindentations were averaged to produce the box plots in Figure 12.

The load frame compliance (mN^{-1}) influences the depth measurement of the indentation. The load frame compliance is the inverse of the spring constant (k) as determined by the Sader method; therefore, each depth measurement will be in error by P/k where P is the load. In order to correct the depth, P/k must be subtracted from all depth measurements, as shown in eq 11.

$$h' = h - \frac{P}{k} \tag{11}$$

The samples studied in this work were MoS_2, ReS_2, $ReSe_2$, and WSe_2. Thin films of a few layers of three of the samples, MoS_2, ReS_2, and $ReSe_2$, were obtained by mechanical tape exfoliation, while thin films of WSe_2 were prepared using chemical vapor deposition. All of the samples were deposited onto a silicon substrate. The MoS_2 crystals used for this study correspond to the mineral molybdenite provided by SPI Supplies. ReS2 single crystals were synthesized through a chemical vapor transport (CVT) technique using either iodine or excess S as the transport agent. Re (99.997%) and S (99.9995%) powders were sealed in vacuumed quartz ampules and brought up to high temperatures in 15 h. The ampule was kept under a temperature gradient of 100 °C for 7 days, with the cold end maintained at 980 °C and the hot end at 1080 °C. After 7 days,

https://doi.org/10.1021/acs.jpcc.4c03861
J. Phys. Chem. C XXXX, XXX, XXX−XXX

the furnace was shut off, and the ampule was harvested at room temperature. WSe_2 and $ReSe_2$ single crystals were synthesized via a flux method: for example, Re (99.997%) and Se (99.9999% powders) in a 1:25 ratio were sealed in quartz ampule, brought to 1050 °C and cooled down to 450 °C in 600 h, to have the crystals centrifuged from the flux. The samples were analyzed under a scanning electron microscope (SEM) and AFM to ensure that there were no significant defects.

Initial estimates of Young's modulus were obtained through AtomicJ.[18] A Python code was developed by our group to allow more flexibility in the curve-fitting procedure and more accurate identification of the contact point. The Python code used in the calculation of Young's modulus and stiffness is available upon request.

RESULTS AND DISCUSSION

Figure 7 shows an AFM image and height profile of an indentation made in a sample of MoS_2. The image was processed in Matlab. The data was initially detrended along the *y*-axis by fitting a second-order polynomial. A Gaussian window was applied to filter high-frequency noise in the image. The depth of the indentation is estimated to be 22 nm. This estimation was determined by finding the minimum value of the image after setting the median value of the image to zero.

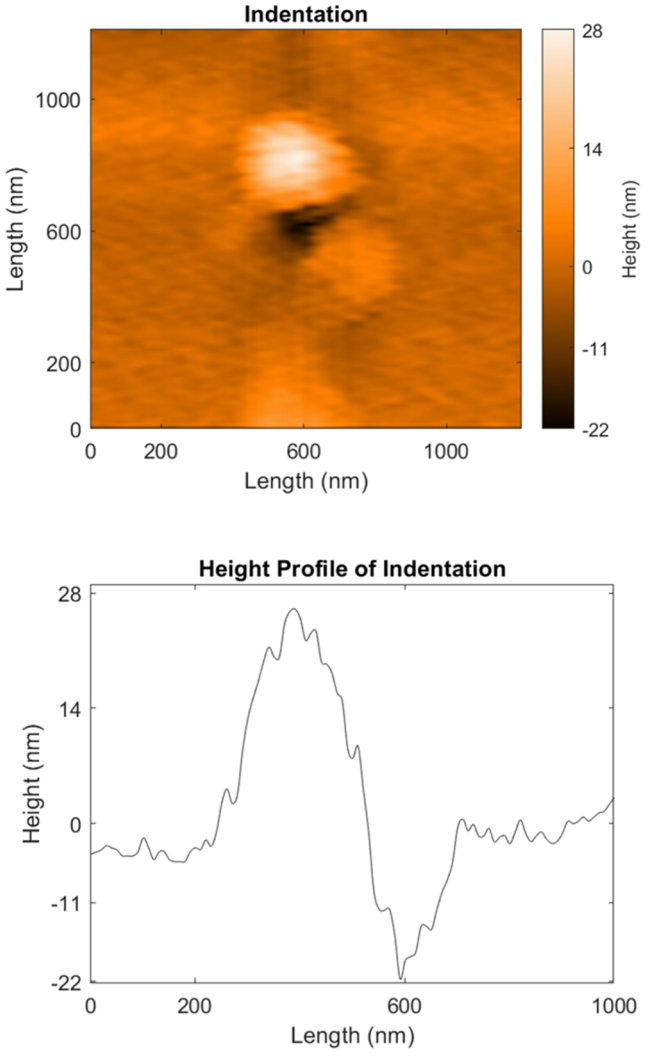

Figure 7. AFM image and height profile of a singular indentation made in a sample of MoS_2. The estimated depth of the indentation is 22 nm.

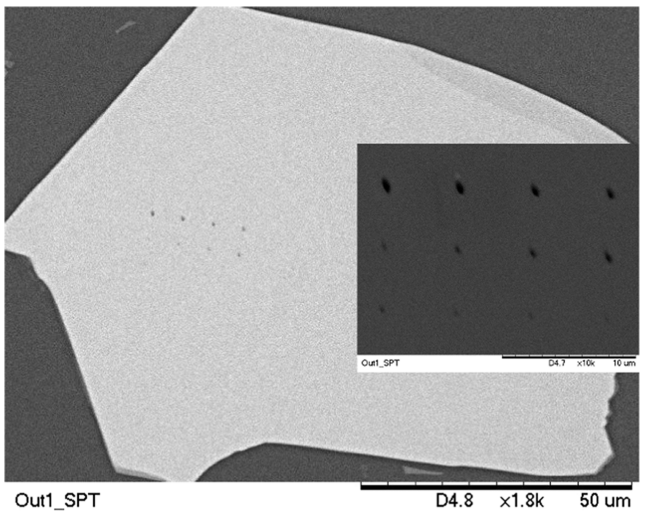

Figure 8. Scanning electron microscope (SEM) image of a sample of MoS_2 after performing 16 indentations. The insert has been enlarged to show 12 of the clearest indentations.

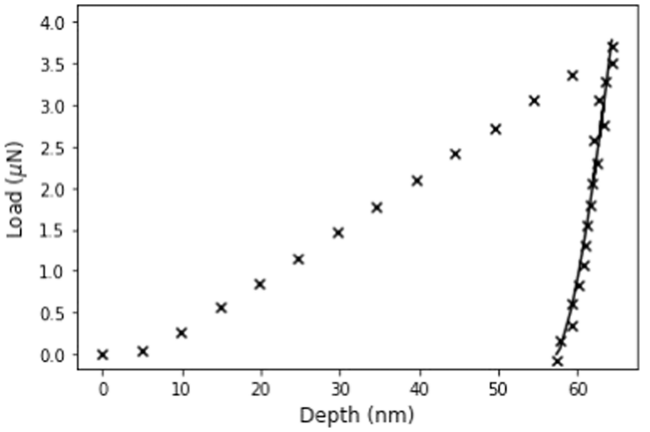

Figure 9. Force−distance curve for MoS_2. The unloading curve has been fit using eq 2.

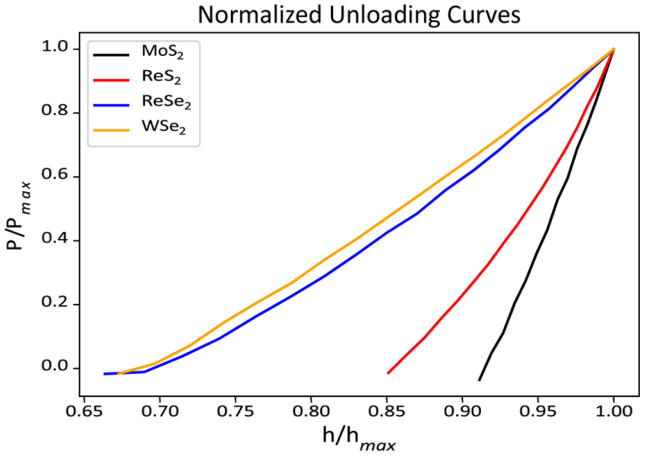

Figure 10. Normalized force−distance curves for MoS_2, ReS_2, $ReSe_2$, and WSe_2.

https://doi.org/10.1021/acs.jpcc.4c03861
J. Phys. Chem. C XXXX, XXX, XXX−XXX

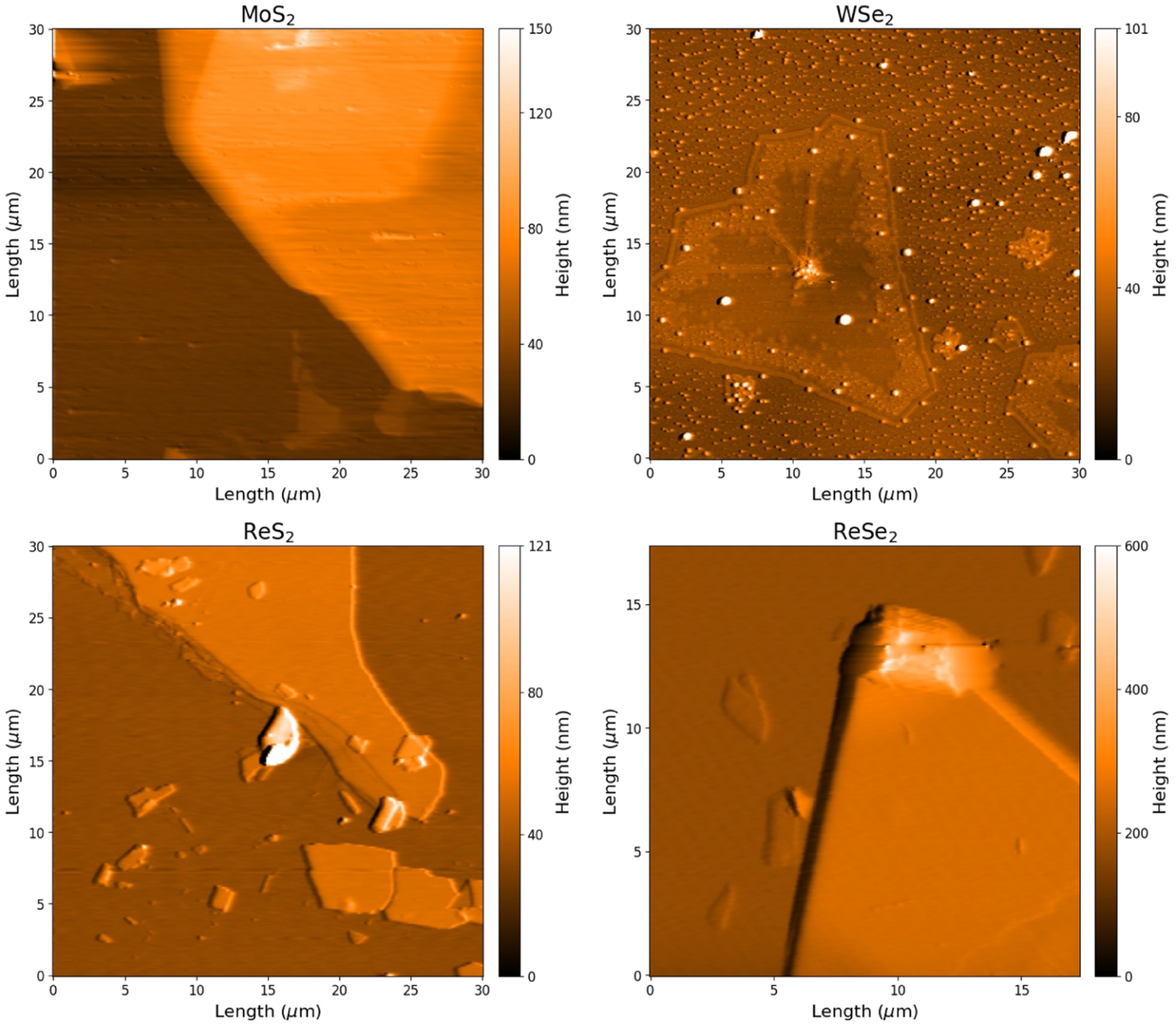

Figure 11. AFM scan images of MoS_2, ReS_2, $ReSe_2$, and WSe_2 samples.

Table 1. Measured Stiffness and Young's Modulus Results for MoS_2, WSe_2, $ReSe_2$, and ReS_2

sample	S (N/m)	E (GPa)
MoS_2	660 ± 260	140 ± 70
WSe_2	290 ± 34	38 ± 9
$ReSe_2$	364 ± 250	37 ± 24
ReS_2	437 ± 130	79 ± 39

Table 2. Young's Modulus of the TMD Samples as Determined by AtomicJ and MountainsSPIP

sample	AtomicJ	MountainsSPIP
MoS_2	131	29
WSe_2	41	12
$ReSe_2$	23	33
ReS_2	73	16

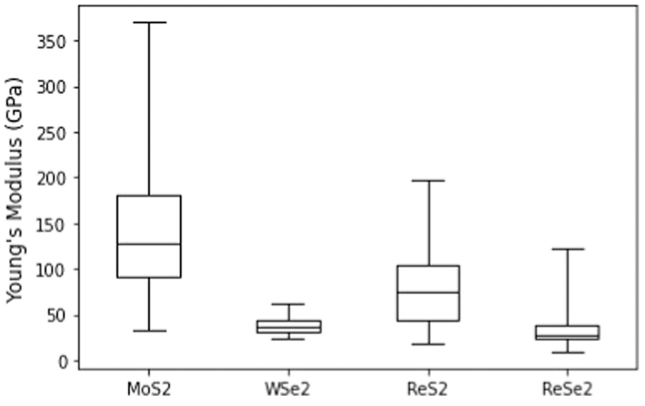

Figure 12. Box plots of the range of values of Young's modulus for each of the samples measured.

There is significant pileup around the indentation which are the brighter regions around the darker indentation in Figure 7. The majority of the pileup is located at the top of the indentation which may indicate that the AFM probe is indenting at an angle. A material's tendency to pile up has largely contributed to higher E/Y (Young's modulus to yield

https://doi.org/10.1021/acs.jpcc.4c03861
J. Phys. Chem. C XXXX, XXX, XXX−XXX

Table 3. Comparison of Our Experimental Young's Modulus Values with Theoretical Calculations for MoS_2, WSe_2, $ReSe_2$, ReS_2, and Their Percent Difference

sample	E (GPa)	$E_{theor.}$ (GPa)	percent difference (%)
MoS_2	140 ± 70	199.525[25]	32
WSe_2	38 ± 9	123.6[26]	106
$ReSe_2$	37 ± 24	66.727[22]	57
ReS_2	79 ± 39	89.243[22]	13

strength) ratios. Materials with ratios greater than 0.7 have been observed to pile up while materials with ratios less than 0.7 have been observed to sink in ref 19. A scanning electron microscope (SEM) image has been taken of one of the indentation locations on MoS_2 in Figure 8. A total of 16 indentations were made in this sample. The SEM image shows 12 of the indentations that could be imaged with the SEM.

Figure 9 shows an expanded view of a force−distance curve data for MoS_2. All four samples exhibited hysteresis and elastic-plastic deformation similar to this curve. While some elastic recovery was observed in the materials, namely $ReSe_2$ and ReS_2, the deformation was mainly plastic. In Figure 10, normalized unloading curves for MoS_2, ReS_2, $ReSe_2$, and WSe_2 have been plotted.

Figure 11 shows the AFM scan images for MoS_2, WSe_2, ReS_2, and $ReSe_2$. The images were imported into Gwyddion to perform mean plane subtraction and scan line level correction.

Table 1 is a summary of the experimental results for the stiffness and reduced Young's modulus obtained through our Python code from the nanoindentation measurements. The calculated uncertainty in Young's modulus is equal to the standard deviation within each set of measurements.

In Table 2, the values of Young's modulus as determined by AtomicJ and MountainsSPIP are shown. Both were fit using Bilodeau's approximation for pyramidal indenters which is shown in eq 12 where ν is Poisson's ratio.[20]

$$P = \frac{1.4906E \tan(\theta)}{2(1-\nu^2)} h^2 \tag{12}$$

Our results show that both MoS_2 and ReS_2 have a higher Young's modulus than $ReSe_2$ and WSe_2. This is in agreement with Falin et al., who found Young's modulus of WS_2 to be approximately 44 GPa greater than WSe_2. Similarly, Deng et al. found WS_2 and MoS_2 to have higher Young's moduli than either WSe_2 or $MoSe_2$ through the first-principles methods.[4,21]

A concise summary of our measured results for Young's moduli of these samples is given in Figure 12 that shows box plots of the data with outliers removed for each of our samples.

Our experimental values for the reduced Young's modulus were compared to those obtained by theoretical calculations by several groups (refs 22−24) as summarized by Table 3.

Our results for Young's modulus of layered samples were lower than those of theoretical calculations and other results

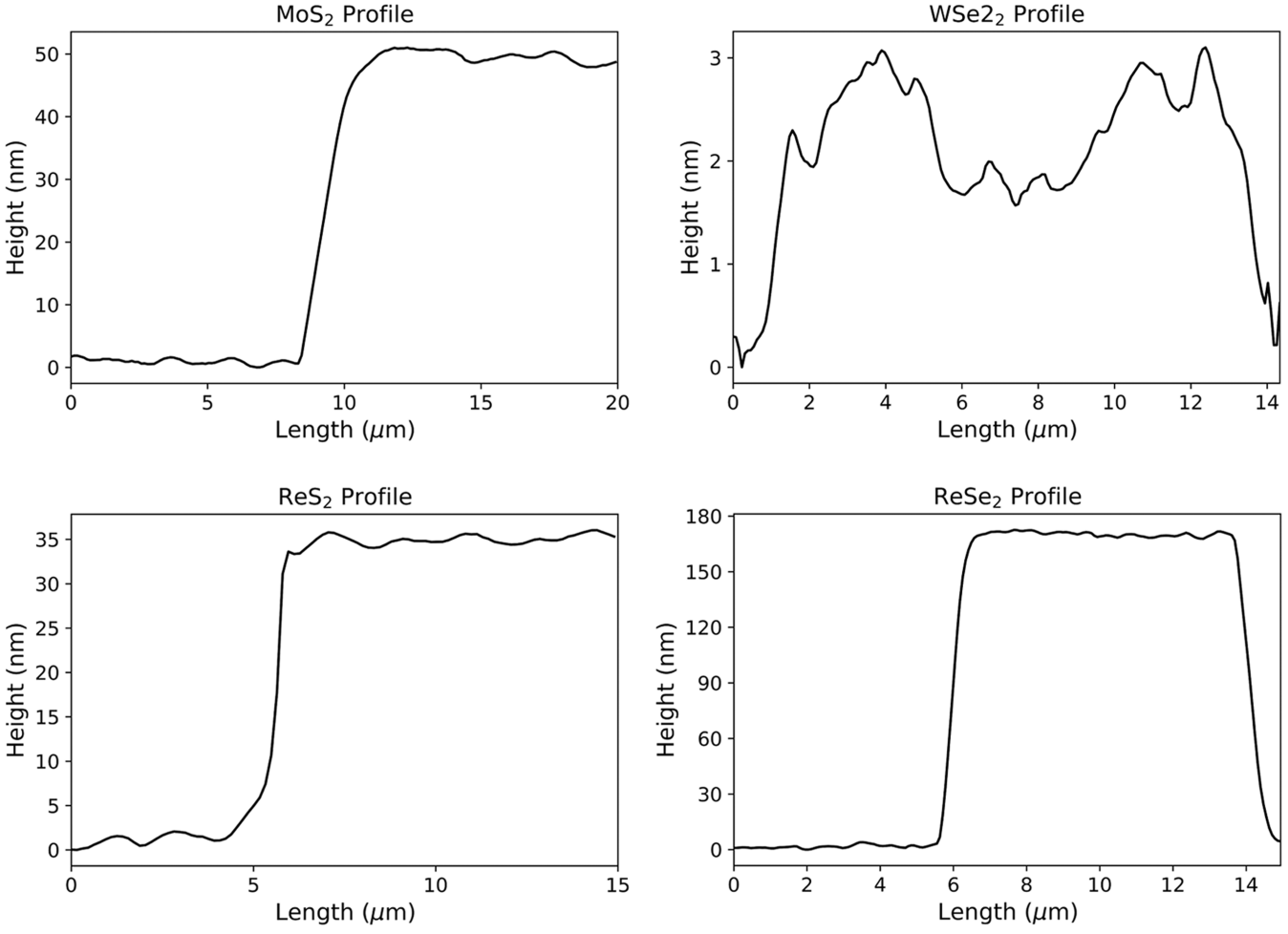

Figure 13. Height profiles of MoS_2, ReS_2, $ReSe_2$, and WSe_2 samples measured by AFM.

https://doi.org/10.1021/acs.jpcc.4c03861
J. Phys. Chem. C XXXX, XXX, XXX−XXX

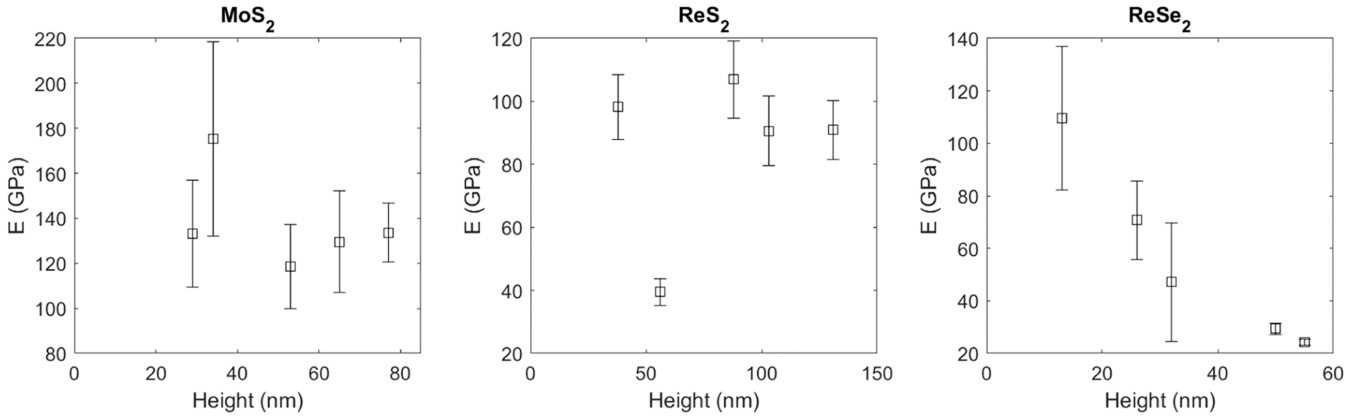

Figure 14. Reduced Young's modulus plotted versus the thickness of the samples. The error bars are the 95% confidence bars.

from nanoindentation of suspended monolayers, as expected. Previous experiments and models have predicted TMDs to be hundreds of GPa. Castellanos-Gomez et al.[23] reported Young's modulus for MoS_2 to be 330 GPa based on nanoindentation of suspended monolayer nanosheets. Cooper et al.[24] used Perdew−Burke−Ernzerhof functional to calculate Young's modulus (E^{2D}) as 129 N/m for 0.615 nm thick monolayer MoS_2 which produces a Young's modulus of approximately 210 GPa. To validate their results, Cooper et al. used nanoindentation on suspended MoS_2 nanosheets. Their experimental result for Young's modulus was 210 GPa.[24] In most of these investigations of TMDs, the samples were often less than 30 atomic layers thick or monolayers. However, our MoS_2, ReS_2, and $ReSe_2$ samples all had thicknesses greater than those reported in the investigations above. A profile was taken on the edge of each sample to compare results and measure sample thicknesses accurately. Figure 13 depicts these profiles. For MoS_2, the sample thickness was estimated to be approximately 52 nm. An individual atomic layer for MoS_2 is found to be 0.675 nm thick.[27] Therefore, the MoS_2 samples have approximately 77 atomic layers. Similarly, WSe_2 has an estimated thickness of 2 nm, and each atomic layer is found to be 0.67 nm[27] thick. There are approximately three atomic layers for each WSe_2 sample. ReS_2 has a thickness of 35 nm based on the height profile in Figure 13, and each atomic layer is found to be 0.64 nm thick.[28] Thus, the ReS_2 samples are estimated to have 54 atomic layers. The $ReSe_2$ samples are estimated to be 170 nm thick, and each atomic layer is 0.656 nm thick.[29] The $ReSe_2$ samples are estimated to be 259 atomic layers. The reduced Young's modulus of MoS_2, ReS_2, and $ReSe_2$ has been plotted against sample thickness in Figure 14 From Figure 14, we observe that the values obtained for Young's modulus for some of our samples seem to decrease with increased sample thicknesses. For MoS_2 and ReS_2, the thickness does not have any apparent influence on the measured modulus of reduced Young's modulus. This result is in agreement with the observations of Meganathan[30] that the reduced Young's modulus does not vary significantly for atomic layers greater than 20. However, the thickness has a clear effect on the reduced Young's modulus of $ReSe_2$, increasing by 85 GPa as the thickness decreases from 55 to 13 nm. WSe_2 was not included since it was created using CVD, producing samples of uniform thickness.

Oxidation should not have a significant effect on the results of the study. Falin et al. found that WSe_2 remained stable even after air exposure of 20−40 weeks.[4]

CONCLUSIONS

Young's moduli were determined for four two-dimensional transition metal dichalcogenides (TMDs) namely molybdenum disulfide (MoS_2), rhenium disulfide (ReS_2), rhenium diselenide ($ReSe_2$), and tungsten diselenide (WSe_2). Our results were compared to theoretical calculations and other measurements of the nanomechanical properties of TMDs represented in Table 3. Values of reduced Young's modulus for some of these TMDs were found to be comparable to those of stainless steel, about 200 GPa. The measured values of Young's modulus and the measured stiffness values are in good agreement with theoretical predictions. The results from the SEM do not show any stacking faults or significant defects in the samples.

ASSOCIATED CONTENT

Supporting Information

The Supporting Information is available free of charge at https://pubs.acs.org/doi/10.1021/acs.jpcc.4c03861.

The Python code has been uploaded as "Supporting information for Publication," with each page consisting of the following: S1: Title of the paper and the names and affiliations of all the authors. S2−S3: Description of the Python code. S4−S20: the Python code itself. A detailed description of the Python Code has been included in the "Supporting Information for Publication". The Python Code for Nanoindentation Analysis program referenced in this paper imports raw data captured by the Nanosurf AFM and attempts to analyze using the Oliver Pharr model. Included in the program are subroutines to correct for potential tilts in baselines, correct for indentation taking into consideration the stiffness and bending of the cantilever, as well as filters to clean up the data. Other options include the zeroing of the contact point, showing the in-contact portion of the data, whether during the loading or unloading process, and its related point of minimum load. The upper 80% of the force−distance curve is extracted from the deflection data to find the contact point. Finally, the program allows for outputs in the. csv format while removing outliers. Reportable data includes contact point depth, stiffness, area, maximum load, minimum load, reduced Young's modulus, final depth, hardness, backward pause, and forward pause (PDF)

https://doi.org/10.1021/acs.jpcc.4c03861
J. Phys. Chem. C XXXX, XXX, XXX−XXX

AUTHOR INFORMATION

Corresponding Author

Luis Balicas − *National High Magnetic Field Laboratory, Tallahassee, Florida 32312, United States; Department of Physics, Florida State University, Tallahassee, Florida 32306, United States;* orcid.org/0000-0002-5209-0293; Email: teklua@cofc.edu

Authors

Alem Teklu − *Department of Physics and Astronomy, College of Charleston, Charleston, South Carolina 29424, United States;* orcid.org/0000-0002-1524-2323

Noah Kern − *Department of Physics and Astronomy, College of Charleston, Charleston, South Carolina 29424, United States*

Narayanan Kuthirummal − *Department of Physics and Astronomy, College of Charleston, Charleston, South Carolina 29424, United States*

Joe Tidwell − *Department of Physics and Astronomy, College of Charleston, Charleston, South Carolina 29424, United States*

Maxwell Rabe − *Department of Physics and Astronomy, College of Charleston, Charleston, South Carolina 29424, United States*

Yu Gong − *Department of Physics and Astronomy, College of Charleston, Charleston, South Carolina 29424, United States;* orcid.org/0000-0002-9357-9503

Wenkai Zhang − *National High Magnetic Field Laboratory, Tallahassee, Florida 32312, United States; Department of Physics, Florida State University, Tallahassee, Florida 32306, United States*

Complete contact information is available at: https://pubs.acs.org/10.1021/acs.jpcc.4c03861

Notes

The authors declare no competing financial interest.

ACKNOWLEDGMENTS

This work was partially supported by the Department of Physics and Astronomy and the School of Sciences, Mathematics, and Engineering at the College of Charleston. The work was also supported by NSF/EPSCoR: SC EPSCoR/IDeA, Award no. 0IA-1655740. L.B. acknowledges support from the US-NSFDMR 2219003 (heterostructure fabrication) and the Office Naval Research DURIP Grant 11997003 (stacking under inert conditions). L.B. also acknowledges support from the National High Magnetic Field Laboratory, which the National Science Foundation supports through NSF/DMR-2128556 and the State of Florida.

REFERENCES

(1) Li, X.; Zhu, H. Two-dimensional MoS_2: Properties, preparation and applications. *J. Materiomics* **2015**, *1*, 33−44.

(2) Yang, S.; Wang, C.; Sahin, H.; Chen, H.; Li, Y.; Li, S.-S.; Suslu, A.; Peeters, F. M.; Liu, Q.; Li, J.; Tongay, S. Tuning the Optical, Magnetic, and Electrical Properties of $ReSe_2$ by Nanoscale Strain Engineering [abstract]. *Nano Lett.* **2015**, *15*, 1660−1666. PMID: 25642738.

(3) Xiong, Y.; Chen, H.; Zhang, D. W.; Zhou, P. Electronic and Optoelectronic Applications Based on ReS_2. *Phys. Status Solidi RRL* **2019**, *13*, No. 1800658.

(4) Falin, A.; Holwill, M.; Lv, H.; Gan, W.; Cheng, J.; Zhang, R.; Qian, D.; Barnett, M. R.; Santos, E. J. G.; Novoselov, K. S.; Tao, T.; Wu, X.; Li, L. H. Mechanical Properties of Atomically Thin Tungsten Dichalcogenides: WS_2, WSe_2, and WTe_2. *ACS Nano* **2021**, *15*, 2600−2610. PMID: 33503379.

(5) Choi, W.; Choudhary, N.; Han, G. H.; Park, J.; Akinwande, D.; Lee, Y. H. Recent development of two-dimensional transition metal dichalcogenides and their applications. *Mater. Today* **2017**, *20*, 116−130.

(6) Zhou, H.; Wang, C.; Shaw, J. C.; Cheng, R.; Chen, Y.; Huang, X.; Liu, Y.; Weiss, N. O.; Lin, Z.; Huang, Y.; Duan, X. Large Area Growth and Electrical Properties of p-Type WSe_2 Atomic Layers. *Nano Lett.* **2015**, *15*, 709−713.

(7) Zhang, Y.; Pan, C. Measurements of mechanical properties and number of layers of graphene from nano-indentation. *Diamond Relat. Mater.* **2012**, *24*, 1−5.

(8) Lee, C.; Wei, X.; Kysar, J. W.; Hone, J. Measurement of the Elastic Properties and Intrinsic Strength of Monolayer Graphene. *Science* **2008**, *321*, 385−388.

(9) Duan, Y.; Stinespring, C. D.; Chorpening, B. Electronic Structures, Bonding Configurations, and Band-Gap-Opening Properties of Graphene Binding with Low-Concentration Fluorine. *ChemistryOpen* **2015**, *4*, 642−650.

(10) Ataca, C.; Şahin, H.; Ciraci, S. Stable, Single-Layer MX_2 Transition-Metal Oxides and Dichalcogenides in a Honeycomb-Like Structure [abstract]. *J. Phys. Chem. C* **2012**, *116*, 8983−8999.

(11) Kolobov, A. V.; Tominaga, J. *Two-Dimensional Transition-Metal Dichalcogenides*, 1st ed.; Springer: Cham, 2016; p 538.

(12) Oliver, W.; Pharr, G. An improved technique for determining hardness and elastic modulus using load and displacement sensing indentation experiments. *J. Mater. Res.* **1992**, *7*, 1564.

(13) Oliver, W.; Pharr, G. Measurement of hardness and elastic modulus by instrumented indentation: Advances in understanding and refinements to methodology. *J. Mater. Res.* **2004**, *19*, 3.

(14) Nix, W. D. Elastic and plastic properties of thin films on substrates: nanoindentation techniques. *Mater. Sci. Eng.: A* **1997**, *234*−*236*, 37−44.

(15) Nanosurf, Nanosurf FlexAFM Operating Instructions for Easyscan 2. 2017; https://www.nanosurf.com/en/.

(16) Sader, J. E.; Larson, I.; Mulvaney, P.; White, L. R. Method for the calibration of atomic force microscope cantilevers. *Rev. Sci. Instrum.* **1995**, *66*, 3789−3798.

(17) Instruments, J. A Practical Guide to AFM Force Spectroscopy. https://www.bruker.com/en/products-and-solutions/microscopes/bioafm/resourcelibrary/a-practical-guide-to-afm-force-spectroscopy-and-data-analysis.html, 2008.

(18) Hermanowicz, P.; Sarna, M.; Burda, K.; Gabrýs, H. AtomicJ: An open source software for analysis of force curves. *Rev. Sci. Instrum.* **2014**, *85*, No. 063703.

(19) Kværndrup, F. B.; Engelbrekt, C.; Omer, C. K.; Somers, M. A.; Chris- tiansen, T. L.; Winther, G. Area determination with pile-up and sink-in in nanoindentation of oxygen containing titanium. *Mater. Today Commun.* **2022**, *30*, No. 103218.

(20) Hermanowicz, P. AtomicJ User's Manual. https://master.dl.sourceforge.net/project/jrobust/1.4/AtomicJ_Users_Manual.pdf?viasf=1, 2021.

(21) Deng, S.; Li, L.; Li, M. Stability of direct band gap under mechanical strains for monolayer MoS_2, $MoSe_2$, WS_2 and WSe_2. *Phys. E* **2018**, *101*, 44−49.

(22) Zhao, Q.; Guo, Y.; Zhou, Y.; Xu, X.; Ren, Z.; Bai, J.; Xu, X. Flexible and Anisotropic Properties of Monolayer MX_2 (M = Tc and Re; X = S, Se). *J. Phys. Chem. C* **2017**, *121*, 23744−23751.

(23) Castellanos-Gomez, A.; Poot, M.; Steele, G. A.; van der Zant, H. S. J.; Agraït, N.; Rubio-Bollinger, G. Elastic Properties of Freely Suspended MoS_2 Nanosheets. *Adv. Mater.* **2012**, *24*, 772−775.

(24) Cooper, R. C.; Lee, C.; Marianetti, C. A.; Wei, X.; Hone, J.; Kysar, J. W. Nonlinear elastic behavior of two-dimensional molybdenum disulfide. *Phys. Rev. B* **2013**, *87*, No. 035423.

(25) Wei, L.; Jun-fang, C.; Qinyu, H.; Teng, W. Electronic and elastic properties of MoS_2. *Phys. E* **2010**, *405*, 2498−2502.

(26) Feng, L.-p.; Li, N.; hao Yang, M.; tang Liu, Z. Effect of pressure on elastic, mechanical and electronic properties of WSe_2: A first-principles study. *Mater. Res. Bull.* **2014**, *50*, 503−508.
(27) Benameur, M. M.; Radisavljevic, B.; Héron, J. S.; Sahoo, S.; Berger, H.; Kis, A. Visibility of dichalcogenide nanolayers. *Nanotechnology* **2011**, *22*, No. 125706.
(28) Miao, P.; Qin, J.-K.; Shen, Y.; Su, H.; Dai, J.; Song, B.; Du, Y.; Sun, M.; Zhang, W.; Wang, H.-L.; Xu, C.-Y.; Xu, P. Unraveling the Raman Enhancement Mechanism on 1T'-Phase ReS_2 Nanosheets. *Small* **2018**, *14*, No. e1704079.
(29) Wolverson, D.; Crampin, S.; Kazemi, A.; Ilie, A.; Bending, S. Raman Spectra of Monolayer, Few-Layer, and Bulk $ReSe_2$: An Anisotropic Layered Semiconductor. *ACS Nano* **2014**, *8*, 11154.
(30) Meganathan, K.; Mangamma, G.; Swaminadhan, M. J.; Murugan, V.; Shinde, N. B.; Ghosh, S.; Eswaran, S. K. Thickness-Dependent Nanoscale Elastic Stiffening of Chemical Vapor Deposited Atomically Thin 2H-MoS_2 Films. *J. Phys. Chem. Lett.* **2024**, *15*, 4206−4211.

https://doi.org/10.1021/acs.jpcc.4c03861
J. Phys. Chem. C XXXX, XXX, XXX−XXX